Full Paper

Photocatalysis

Trifunctional Cu-Mesh/Cu_2O@FeO-nanoarrays for highly efficient degradation of antibiotic, inactivation of antibiotic-resistant bacteria and damage of antibiotics resistance genes

Long Zhao, Wei Zhou, Ming Wen, Qingsheng Wu, Weiying Li,* Yongqing Fu, Quanjing Zhu, Sheng Chen, Jiaqi Ran*

L. Zhao, Dr. W. Zhou, Prof. M. Wen, Prof. Q. S. Wu, Prof. W. Y. Li, Dr. Q. J. Zhu, Dr. S. Chen, J. Q. Ran

School of Chemical Science and Engineering, College of Environmental Science and Engineering,

Shanghai Key Laboratory of Chemical Assessment and Sustainability,

State Key Laboratory of Pollution Control and Resource Reuse,

Tongji University, Shanghai 200092, China

E-mail: m_wen@tongji.edu.cn

Prof. Y. Fu

Faculty of Engineering and Environment,

Northumbria University,

Newcastle upon Tyne NE99, UK

Keywords: Cu-Mesh/Cu_2O@FeO-nanoarrays, antibiotic, antibiotic resistant bacteria, antibiotic resistance genes, photocatalytic degradation

Abstract:

Trifunctional Cu-mesh/Cu_2O@FeO-nanoarrays heterostructure is designed and fabricated by integrating Cu_2O@FeO-nanoarrays onto Cu-mesh (CM) *via* an *in situ* growth and phase-transformation process. It is successfully applied to efficiently mitigate the antibiotic pollution, including degradation of antibiotics, inactivation of antibiotic-resistant bacteria (ARB) and damage of antibiotics resistance genes (ARGs). Under visible-light irradiation, CM/Cu_2O@FeO-nanoarrays exhibits a superior degradation efficiency on antibiotics (e.g., up

to 99% in 25 min for tetracycline hydrochloride, TC), due to the generated reactive oxygen species (ROS), especially the dominant $\cdot O^{2-}$. It can fully inactivate *E. coli* (HB101) with initial number of ~10^8 CFU·mL^{-1} in 10 min, which is mainly attributed to the synergistic effects of 1D nanostructure, dissolved metal ions and generated ROS. Meanwhile it is able to damage ARGs after 180 min of photodegradation, including *tetA* (*vs.* TC) of 3.3 $\log_{10}$, *aphA* (*vs.* kanamycin sulfate, KAN) of 3.4 $\log_{10}$, and *tnpA* (*vs.* ampicillin, AMP) of 4.4 $\log_{10}$, respectively. This work explores a green way for treating antibiotic pollution under visible-light.

1. Introduction

Since the discovery of antibiotics in 1928, their usage in treatment of human and animal diseases has been increased exponentially world-wide.[1] However, the improper use of antibiotics has caused severe problems in an aquatic environment, such as accumulation of antibiotics,[2,3] enrichment of antibiotic-resistant bacteria (ARB) and their related antibiotics resistance genes (ARGs).[4,5] Moreover, ARGs can be spread vertically and horizontally in the water polluted by antibiotics, thus producing new generations of resistant genes and exchanging resistant genes among different bacterial species.[6] This will increase the antibiotic resistance and reduce the effectiveness of therapeutic drugs.[7] Thus, it is urgently required to search highly efficient pathways to solve antibiotic pollutions, including degradation of antibiotics, inactivation of ARB, and damage of ARGs. Among these methods, advanced oxidation processes (AOPs) utilize solar energy to oxidize macromolecular pollutants in water and degrade them into low toxic or non-toxic small molecular substances.[8,9] This can be achieved by converting natural and abundant O_2 into $\cdot O^{2-}$[10] which is one type of reactive oxygen species (ROS) with the optimal oxidizability. This method is a promising green way for solving the antibiotics pollutions.

Recently, semiconductor photocatalysis technology has also been explored, since it can effectively utilize the conduction-band electrons (e^-) and valence-band holes (h^+) generated

by solar energy to promote the production of ROS for solving antibiotic pollution.[11,12] Among different semiconductor materials, cuprous oxide (Cu_2O) with its optimal conduction band (CB) of -0.28 eV and valence band (VB) of 1.92 eV presents a prominently antibacterial function under the visible-light.[13,14] Unfortunately, there is a severe photo-corrosion effect for the Cu_2O, which causes the poor stability of Cu_2O based photo-catalyst.[15] Different efforts have been made to solve this issue, and constructing a heterostructure of Cu_2O by adding first-row transition metals is considered to be one of the most potential approaches.[16] Based on the good biocompatibility of element Fe,[17] zero-valence iron and iron oxides have been introduced to enhance the stability of Cu_2O by constructing heterojunction.[18] Especially, FeO possesses the E_{CB} value of -0.17 eV,[19] which can promote the conversion of H_2O_2 into ·OH to degrade organic pollutants in water under the visible-light.[20,21] So, FeO may be a promising candidate to combine with Cu_2O for treating antibiotic pollution *via* enlarging the photo-responsive range of visible-light. Additionally, one-dimensional (1D) nanostructure with a high aspect ratio and a vertical orientation can not only improve the absorption and scattering of visible-light,[22] but also facilitate the charge carrier transport.[23] Therefore, it can greatly enhance the photocatalytic performance. It is worth noting that the tips of these 1D nanomaterials have sharp tips which can pierce through the cell membrane, causing the content to flow out and then be killed when they come into contact with bacteria. In nature, there are nanorod array structures on the surface of cicada wings. These nanorods are like neatly arranged steel needles which will lead to the mechanical rupture of the cell wall of bacterial cells attached to them.[24] Two-dimensional (2D) metal substrates with large specific surface areas are often used as carrier collectors and directional transport platforms.[25-27] Therefore, if the 1D nanostructure can be vertically integrated onto the 2D metal substrate to form a multi-dimensional heterostructure, its visible-light contact area and utilization efficiency can be dramatically improved.[28-30]

In this work, 1D Cu_2O@FeO-nanoarrays heterostructure was integrated onto a 2D Cu-mesh (CM) through *in situ* growth and phase transformation (GPT) process. Cu_2O@FeO-nanoarrays can remarkably promote the generation of e^--h^+ pairs by enhancing the absorption and scattering of visible-light. Meanwhile the directional transport of 2D CM can effectively separate the generated carriers, thus facilitating the ROS effect (especially conversion of· nature O_2 into $\cdot O^{2-}$), which can dramatically enhance the photocatalytic activities of antibiotics and ARGs. Additionally, the "tip recognition" effect of 1D Cu_2O@FeO-nanoarrays is favorable for the inactivation of ARB by destroying the cell wall and exposing its internal structures.[18] Therefore, based on the above discussions, trifunctional CM/Cu_2O@FeO-nanoarrays can achieve a rapid degradation of antibiotics (including tetracycline hydrochloride, TC; ampicillin, AMP; kanamycin sulfate, KAN), the inactivation of *Escherichia coli* (*E. coli*) HB101 and damage of ARGs (*tetA vs.* TC, *aphA vs.* AMP, and *tnpA vs.* KAN) under visible-light irradiation. This study provides a green approach to solve the problem of antibiotics pollution, which is crucial for the effective restoration of ecological environment.

2. Results and discussion

2.1. Morphologies and Structures

Figure 1 shows the formation mechanisms of as-designed CM/Cu_2O@FeO-nanoarrys photocatalyst and control group samples obtained *via* the different pathways. Firstly, Cu^{2+} ions dissolved from CM (by the action of $S_2O_8^{2-}$) reacted with OH^- to form CM/$Cu(OH)_2$-nanoarrays *via* an *in situ* growth process (Text S1, Supporting information, SI). Then $Fe(OH)_3$ colloids were obtained using a hydrolysis process by attaching Fe^{3+} onto $Cu(OH)_2$-nanoarrays to form CM/$Cu(OH)_2$@$Fe(OH)_3$-nanoarrays (Text S2, SI). The subsequent *in situ* phase transformation process, CM/Cu_2O@FeO-nanoarrays (path 1) and CM/Cu_2O@Fe_2O_3-nanoarrays (path 2) were produced in different atmospheres. Besides, CM/Cu_2O-nanoarrays was obtained from CM/$Cu(OH)_2$-nanoarrays by heating treatment at 400 ℃ for 2 h under N_2.

As following, deposition of Fe^0 *via* the reduction of Fe^{2+} by $NaBH_4$ gave rise to CM/Cu_2O@Fe-nanoarrays (path 3, Text S3, SI). In addition, optical images of different products grown on CM are shown in Figure 1 (bottom left). The color of the sample surface is changed from yellow (CM) to blue (CM/$Cu(OH_2)$) and then to brown (CM/Cu_2O-FeO) or black (CM/Cu_2O-Fe_2O_3) corresponding to path 1 or path 2, respectively. Simultaneously, the CM/$Cu(OH_2)$ with blue changed to orange red (CM/Cu_2O) and then dark brown (CM/Cu_2O-Fe) corresponding to path 3. The morphological changes of obtained products by different synthesis processes were monitored by scanning electron microscope (SEM, Figure S1 in Supporting Information, SI). It can be observed that control group samples of CM/Cu_2O, CM/Cu_2O-Fe, and CM/Cu_2O-Fe_2O_3 with the corresponding average diameters of 200, 410, and 550 nm, and that the original nanoarray structures can be maintained after being coated with Fe and Fe_2O_3.

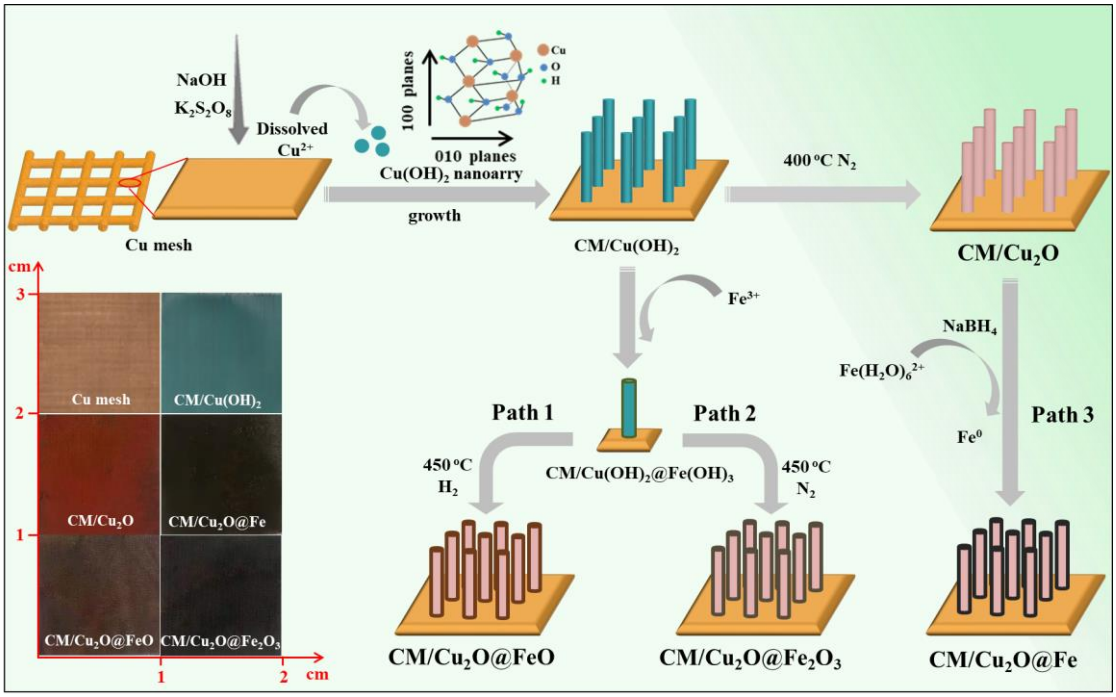

Figure 1. Synthesis schematic views for as-designed CM/Cu_2O@FeO-nanoarrays heterostructures and the control group samples with their inset optical images.

Figure 2 shows images of CM/Cu_2O@FeO-nanoarrays obtained by using SEM and transmission electron microscope (TEM). The diameter of Cu fibers in the Cu_2O@FeO-

nanoarrays is increased from their original diameter of ~ 50 μm into ~100 μm (Figure S2, SI). So the length of nanoarrays is ~25 μm (Figure 2A). The average diameter of Cu_2O@FeO-nanoarrays is ~400 nm with a dense layer of FeO nanoparticles covered on the surface of Cu_2O-nanoarrays (Figure 2B and C). It can be observed that the lattice fringes have the spacing of 0.19 nm for FeO (211) planes and 0.20 nm for Cu_2O (111) planes in high resolution TEM (HR-TEM) image (Figure 2D). The formation of CM/Cu_2O@FeO nanostructures can be further confirmed by the selective area electron diffraction (SAED) pattern (inset of Figure 2D). The lattice fringes clearly show apparent changes in their orientations at the phase interface between Cu_2O and FeO (marked in circle), which indicates the formation of heterojunctions.[31]

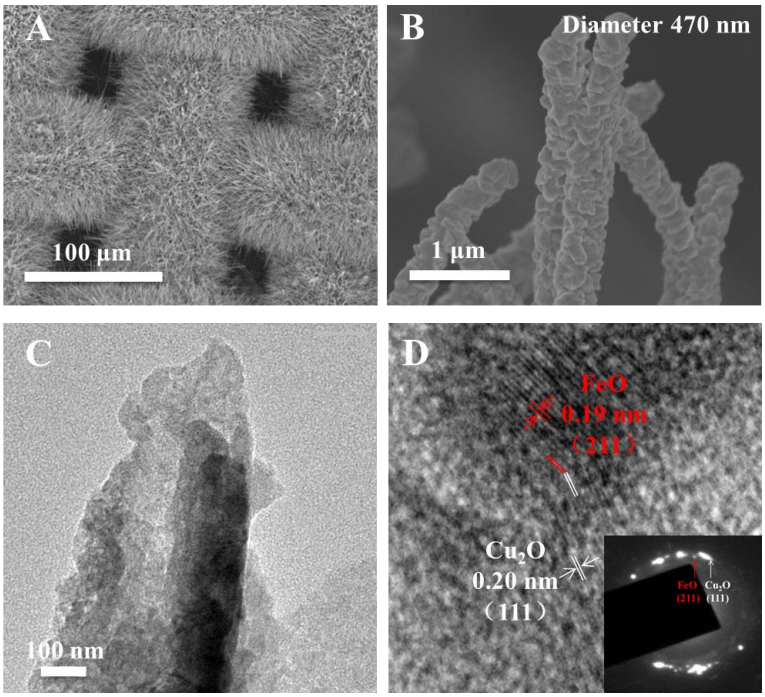

Figure 2. (A, B) Low and high magnification SEM images; (C) TEM image; (D) HR-TEM image with inset SAED pattern of the CM/Cu_2O@FeO-nanoarrays.

Figure 3 illustrates the characterization of composition and phase-structure. As shown in energy dispersive X-ray spectroscopy (EDS) in Figure 3A, Cu and O are the major elements in CM/Cu_2O while Fe element appears in CM/Cu_2O@Fe, CM/Cu_2O@FeO, and CM/Cu_2O@Fe_2O_3. In addition, the peak area ratio of O element in the CM/Cu_2O@Fe is

almost the same as that of CM/Cu_2O, which indicates the possible formation of zero-valent iron (Fe^0). The peak area ratios of O element for the CM/Cu_2O@FeO and CM/Cu_2O@Fe_2O_3 are much larger than those of CM/Cu_2O and CM/Cu_2O@Fe, due to the existence of iron oxides (Table S1, SI). As observed in X-ray diffraction (XRD) patterns (Figure 3B), the diffraction peaks at 2θ = 43.32°, 50.44° and 74.12° are corresponding to the planes of (111), (200), and (220) Cu crystal (JCPDS no. 65-9026).[32] While those peaks at 36.48°, 42.38°, 61.43°, and 73.53° match well with the (111), (200), (220), and (311) lattice planes of Cu_2O (JCPDS no. 65-3288).[33] Additionally, the diffraction peaks at 2θ = 42.32°, 45.31°, 48.35°, 63.32°, and 77.42° are indexed to the (100), (002), (101), (102), and (110) lattice planes of Fe^0 (JCPDS no. 65-5099).[34] Simultaneously, those peaks at 35.56°, 37.71°, 43.62°, 61.37°, and 73.51° are indexed to the (003), (101), (102), (104), and (105) lattice planes of FeO (JCPDS no. 39-1088).[35] Meanwhile, peaks at 24.14°, 33.25°, 35.67°, 38.86°, and 48.95° are corresponding to the (110), (211), (1-10), (222), and (220) lattice planes of Fe_2O_3 (JCPDS no.85-0987).[36] Therefore, the crystal structures of copper oxides and iron oxides in the as-obtained materials can be confirmed as Cu_2O, FeO, and Fe_2O_3. Figure 3C shows the Raman spectra of different samples. For the CM/Cu_2O, the peaks at 214, 297, 443, and 627 cm^{-1} are assigned to the characteristic vibrations of Cu-O.[37,38] It can be observed that the peak of 443 cm^{-1} is shifted to the 406 cm^{-1} in CM/Cu_2O@FeO due to formation of heterojunctions at the interfaces between FeO and Cu_2O.[39] In order to investigate the light response of as-designed photocatalyst, UV-vis diffuse reflectance spectra are measured and shown in Figure 3D. Both CM/Cu_2O@Fe_2O_3 and CM/Cu_2O@FeO exhibit better photo-responses than the CM/Cu_2O in the visible-light region (550 ~ 650 nm). Therefore, the introduction of FeO and Fe_2O_3 can enhance the catalytic performance by promoting the generation of e^--h^+ pairs in the photocatalytic process. In order to further understand the band gap information, the band gap and valence band energy values of CM/Cu_2O and CM/Cu_2O@FeO were calculated by Equation (1) and (2).[40]

$$(\alpha h\nu)^{1/n} = A(h\nu - E_g) \quad (1)$$

$$E_{CB} = E_{VB} - E_g \quad (2)$$

where α is the absorption index, h is the Planck constant, ν is the frequency, A is a constant. E_g, E_{CB}, and E_{VB} are the band gap, valence band, and conduction band of semiconductor, respectively.

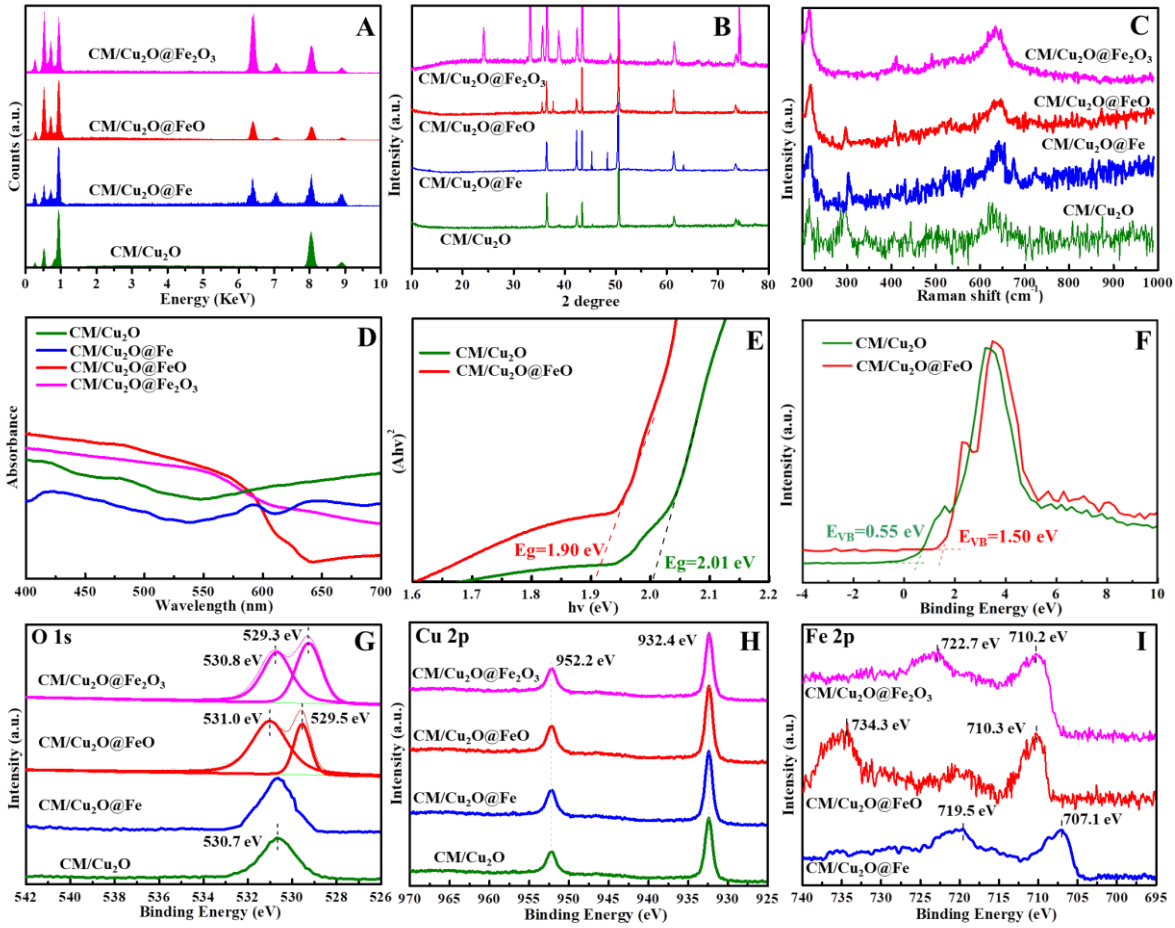

Figure 3. (A) EDS spectra; (B) XRD patterns; (C) Raman spectra; (D) UV-vis diffuse reflectance spectra; (E) bandgap energy; (F) VXPS spectra; (G) - (I) XPS detail spectra of O 1s, Cu 2p, and Fe 2p for the prepared samples.

As shown in Figure 3E, the band gap energy values of CM/Cu_2O and CM/Cu_2O@FeO are 2.01 and 1.90 eV. The X-ray photoelectron spectroscopy (XPS) valence band spectra of CM/Cu_2O and CM/Cu_2O@FeO indicated that E_{VB} energy values are 0.55 eV and 1.50 eV (Figure 3F), respectively. Therefore, the E_{CB} energy values of CM/Cu_2O and CM/Cu_2O@FeO

nanoarrays can be calculated as -1.46 eV and -0.40 eV, respectively. Thus, the dissolved O_2 in the solution can be transformed into $\cdot O^{2-}$ by the activation of conduction-band electrons because the E_{CB} value of CM/Cu_2O@FeO-nanoarrays is more negative than that of the $O_2/\cdot O_2^-$ potential (-0.33 eV *vs.* NHE).[41] XPS analysis was further employed to know the information of elemental bonding and valence. The XPS survey spectra of CM/Cu_2O@FeO-nanoarrays and the control group samples all show peaks of O 1s, Cu 2p, and Fe 2p (except for CM/Cu_2O, which does not have Fe) (Figure S3, SI). For the O 1s spectra in Figure 3G, the peak at 530.7 eV is assigned to O of Cu-O in CM/Cu_2O and CM/Cu_2O@Fe-nanoarrays[42] while the peaks at 529.5 and 529.3 eV are assigned to Fe-O in CM/Cu_2O@FeO and CM/Cu_2O@Fe_2O_3 nanoarrays, respectively.[43] The binding energy of Cu-O is shifted to 531.0 and 530.8 eV due to the charge redistribution caused by the heterojunction which is formed by the interaction between two oxides of Cu and Fe in CM/Cu_2O@FeO and CM/Cu_2O@Fe_2O_3 nanoarrays.[44] All the four Cu 2p spectra in Figure 3H, the two peaks at 932.4 and 952.2 eV are corresponding to Cu $2p_{3/2}$ and Cu $2p_{1/2}$ which are consistent with those of the CM/Cu_2O [Cu^0/Cu^+].[45] No satellite peaks are identified in Cu 2p spectra suggesting that the materials only contain Cu^+. In Figure 3I, the Fe 2p spectra present two peaks at 719.5 and 707.1 eV which are related to Fe^0 for the CM/Cu_2O@Fe nanoarrays.[46,47] The binding energies of Fe $2p_{1/2}$ and Fe $2p_{3/2}$ at 734.3 & 710.3 eV as well as 722.7 & 710.2 eV can be assigned to Fe^{2+} and Fe^{3+} for CM/Cu_2O@FeO and CM/Cu_2O@Fe_2O_3 nanoarrays, respectively.[48] XPS results confirm the formation of CM/Cu_2O@Fe, CM/Cu_2O@FeO, and CM/Cu_2O@Fe_2O_3.

2.2. Degradation of antibiotic

TC, AMP, and KAN were selected as degradation targets by using designed CM/Cu_2O@FeO and the control group samples as the photocatalysts. Because the proliferation of *E. coli* HB101 is difficult to be inhibited by TC, AMP, and KAN due to the existence of ARGs (*tetA vs.* TC, *aphA vs.* KAN, *tnpA vs.* AMP).[49-51] The obtained results are

shown in **Figure 4**. There are almost no apparent degradation (less than 2%) or minor degradation (~ 10%) under dark and visible-light irradiation conditions for all three antibiotic solutions without applying any catalysts (e and f in Figure 4A-C). Therefore, the selected three antibiotics cannot be degraded effectively and naturally under the visible-light irradiation. Under visible-light irradiation for 25 min, the degradation efficiency toward TC can approach to an optimal value of 99% catalyzed by CM/Cu_2O@FeO-nanoarrays, while the efficiency readings are only 85%, 77%, and 66% for CM/Cu_2O@Fe_2O_3, CM/Cu_2O@Fe, and CM/Cu_2O, respectively (Figure 4A). The similar cases have also been observed for both AMP and KAN.

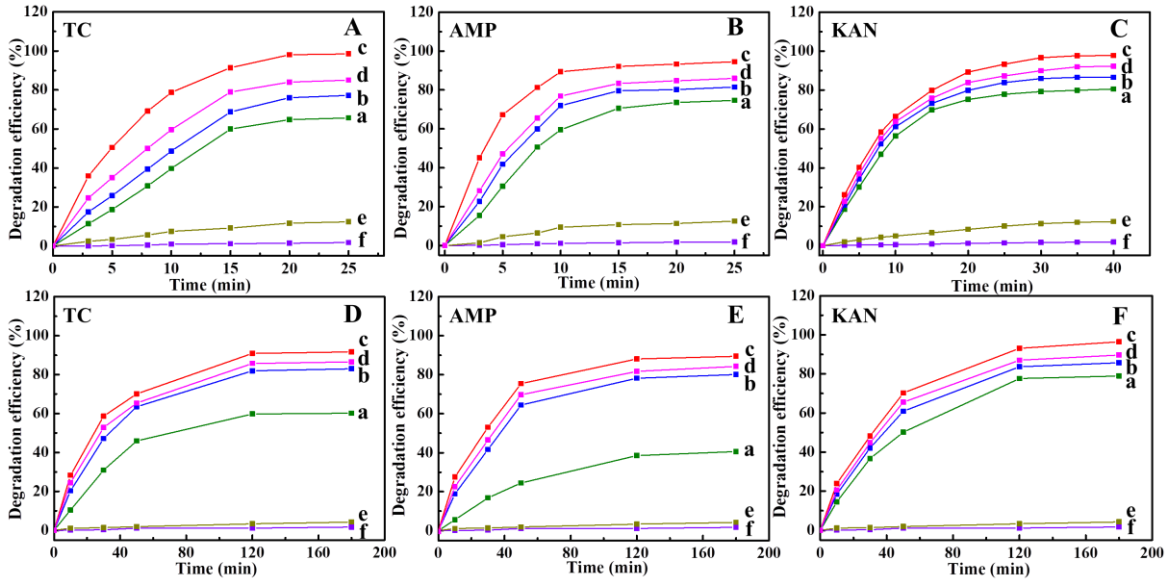

Figure 4. The degradation efficiency of single solution of TC (A), AMP (B), and KAN (C) and mixture solution of TC (D), AMP (E), and KAN (F) for CM/Cu_2O (a), CM/Cu_2O@Fe (b), CM/Cu_2O@FeO (c), CM/Cu_2O@Fe_2O_3 (d); visible-light irradiation without catalysis (e) and dark without catalysis (f).

The degradation efficiency order for AMP is CM/Cu_2O@FeO (95%) > CM/Cu_2O@Fe_2O_3 (86%) > CM/Cu_2O@Fe (81%) > CM/Cu_2O (75%) within 25 min (Figure 4B) and it is CM/Cu_2O@FeO (98%) > CM/Cu_2O@Fe_2O_3 (92%) > CM/Cu_2O@Fe (87%) > CM/Cu_2O (81%) for KAN within 40 min (Figure 4C). These results clearly indicate that the catalytic

activities of these catalysts come mainly from Cu_2O and it is enhanced by Fe or iron oxides with different valences, especially for FeO. In the antibiotics pollution environment, many antibiotics are co-existed.[52] Therefore, the mixed antibiotic solutions of TC, AMP, and KAN were employed to evaluate the degradation activity of the prepared photocatalysts (Figure 4D-F). The antibiotic degradation by using the control groups (e and f) was also carried out under the visible-irradiation and dark conditions without applying any catalysis material. For the control groups, the degradation efficiency values of TC, AMP, and KAN are all less than 2%, indicating that these three antibiotics cannot be effectively degraded naturally under the visible-light irradiation. The CM/Cu_2O@FeO-nanoarrays has the optimal degradation efficiency to each antibiotic in the mixed antibiotic solution. However, compared with the efficiency values for the degradation process in the presence of single antibiotic, the degradation efficiency values in the mixed solutions are slightly decreased and the degradation times are also increased up to 180 min. The degradation efficiencies of CM/Cu_2O@FeO, CM/Cu_2O@Fe_2O_3, CM/Cu_2O@Fe, and CM/Cu_2O in the mixed solutions of TC, AMP, and KAN are shown in **Table 1**. Although multiple antibiotics within the complex environment cause the increase of their degradation time, the final degradation efficiency still reaches about 90% for CM/Cu_2O@FeO-nanoarrays. Compared with the visible-light photocatalytic degradation performance of different materials reported in literature, the degradation efficiency of CM/Cu_2O@FeO-nanoarrays in this study is much higher and degradation time is much shorter (see Table S2, SI).

Table 1. The degradation efficiency for mixture solution of TC, AMP, and KAN.

	CM/Cu_2O	CM/Cu_2O@Fe	CM/Cu_2O@FeO	CM/Cu_2O@Fe_2O_3
TC	60.18%	83.00%	91.64%	86.46%
AMP	40.57%	80.08%	91.64%	86.46%
KAN	78.96%	85.67%	91.64%	89.70%

To fully understand the degradation process, the pseudo-first-order kinetic model is appliedwhich is expressed using the following equation (3):[53]

$$-\ln(C_t/C_0) = kt \quad (3)$$

where C_t, C_0, k and t represent the instant antibiotic concentration, initial antibiotic concentration, rate constant and reaction time, respectively. The linearly fitting results of all the samples using equation (3) are displayed in Figure S4 and the corresponding parameters are listed in Table S3. According to values of k, the CM/Cu_2O@FeO-nanoarrays displays the optimal degradation rates for TC (-0.181 min^{-1}), AMP (-0.114 min^{-1}), and KAN (-0.110 min^{-1}) in a single antibiotic solution. In the mixed antibiotics solution, the CM/Cu_2O@FeO-nanoarrays show optical degradation rates for TC (-0.019 min^{-1}), AMP (-0.008 min^{-1}), and KAN (-0.190 min^{-1}). These simulated results are consistent with the experimental ones.

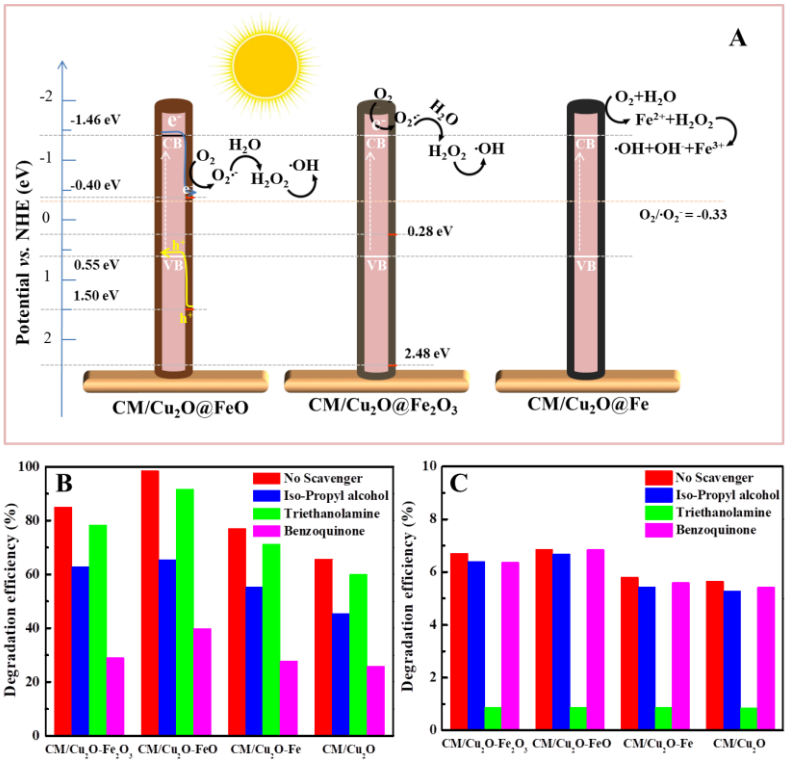

Figure 5. (A) The illustrated mechanism of ROS generation; (B, C) Effects of various quenchers on degradation of TC aerobic and anaerobic conditions, respectively.

There are differences in the antibiotic degradation performance for the as-prepared materials: CM/Cu_2O@FeO > CM/Cu_2O@Fe_2O_3 > CM/Cu_2O@Fe > CM/Cu_2O. In principle,

the photocatalyst is irradiated by the visible-light to generate the e^--h^+ pairs which can be employed to generate ROS from O_2 or H_2O in photodegradation processes.[54] Thus, the above differences in the degradation performance may be caused by the different mechanisms of ROS formation as shown in **Figure 5**A. In the CM/Cu_2O@FeO-nanoarrays, FeO and Cu_2O are *n*-type and *p*-type semiconductors, respectively. The E_{CB} (-1.46 eV) value of Cu_2O is far more negative than that of FeO (-0.40 eV). Thus, e^- will tend to be accumulated in the CB of FeO and h^+ will tend to be accumulated in the VB of Cu_2O, which are driven by the built-in electric field in the heterojunction formed between Cu_2O and FeO, to effectively separate the e^--h^+ pairs. Subsequently, the accumulated e^- reduces O_2 to generate $\cdot O_2^-$ because the E_{CB} of CM/Cu_2O@FeO-nanoarrays is more negative than that of the $O_2/\cdot O_2^-$ potential (-0.33 eV *vs.* NHE).[34] Furthermore, the e^- could react with $\cdot O_2^-$ and H_2O to create ·OH.[55] Meanwhile, the h^+ also reacts directly with antibiotics.[56] These processes can be described using the following Equation (4) to (9):

$$Cu_2O@FeO \rightarrow Cu_2O@FeO(e^-\text{-}h^+) \quad (4)$$

$$Cu_2O@FeO(e^-\text{-}h^+) \rightarrow Cu_2O@FeO(e^-) \quad (5)$$

$$O_2 + e^- \rightarrow \cdot O_2^- \quad (6)$$

$$\cdot O_2^- + H_2O + e^- \rightarrow H_2O_2 \quad (7)$$

$$H_2O_2 + e^- \rightarrow \cdot OH \quad (8)$$

$$\cdot O_2^-/\cdot OH/h^+ + \text{antibiotics} \rightarrow \text{degradation products} \quad (9)$$

The degradation efficiency of CM/Cu_2O@FeO-nanoarrays is the superior among all the as-prepared catalytic materials may be due to the optimal photo-responsive property in the visible-light range. By comparison, Fe_2O_3 cannot generate $\cdot O_2^-$ by reducing O_2 due to its more positive CB than the potential of $O_2/\cdot O_2^-$. CM/Cu_2O@Fe_2O_3-nanoarrays can only rely on the photocatalytic activity of Cu_2O to obtain $\cdot O_2^-$. Besides, Fe_2O_3 may perform as a charge trapping center to promote photocatalytic activity. According to crystal field theory,[57] the d-orbitals of Fe are vacant during the oxidation/reduction reaction processes. Thus, the e^- can be

trapped in the Fe^{3+} center during the process of e^- excited transition in Cu_2O, which suppresses the e^--h^+ recombination. The Fe^0 in the CM/Cu_2O@Fe-nanoarrays can combine with water molecules thus dissolving oxygen to form H_2O_2 and Fe^{2+}. The hydroxyl radicals (·OH) are then formed by oxidation in the presence of visible-light to assist Cu_2O in degrading antibiotics. The reaction process as shown in Equation (10) and (11).[58]

$$Fe^0 + nH_2O + O_2 \rightarrow Fe^{2+} + H_2O_2 \quad (10)$$

$$Fe^{2+} + H_2O_2 \rightarrow Fe^{3+} + OH^- + \cdot OH \quad (11)$$

Nevertheless, the antibiotics can dissolve the Fe ions to form metal complex which is adverse for the degradation of antibiotics.[59] Therefore, the degradation efficiency of CM/Cu_2O@Fe-nanoarrays is slightly lower than that of CM/Cu_2O@Fe_2O_3-nanoarrays. The nanoarray structures also greatly improve the degradation of antibiotics because of the following reasons. (I) Vertical oriented 1D Cu_2O-FeO nanoarrays can not only effectively generate e^--h^+ pairs under the visible-light, but also effectively separate them;[22] (II) 1D nanoarrays with Cu_2O@FeO heterostructure have large effective heterointerfaces which can effectively improve the absorption and scattering of visible-light, thus ensuring the good photocatalytic activity and stability.[60]

To further prove the role of different types of ROSs under visible-light irradiation, the masking experiments of ROS were carried out. As shown in Figure 5B, iso-propyl alcohol (IPA), benzoquinone (BQ), and triethanolamine (TEA) were used to quench ·OH, $\cdot O_2^-$, and H^+ species.[61] The TC is used as a reference. The degradation efficiency of TC is 99% catalyzed by CM/Cu_2O@FeO-nanoarrays without adding any scavenger. After introducing IPA, BQ, and TEA, the degradation efficiencies are decreased to 65%, 92%, and 40%, respectively. The same experiments were carried out when CM/Cu_2O@Fe_2O_3, CM/Cu_2O@Fe, and CM/Cu_2O were used as the photocatalysts. The degradation efficiencies are reduced to 63%, 55%, and 45% from 85%, 77%, and 66% with IPA as the scavenger. If IPA is replaced by BQ (or TEA), the degradation efficiencies are decreased to 29%, 28%, 26% (or 78%, 71%,

and 60%), respectively. The above results demonstrate that $\cdot O_2^-$ radicals are the dominant species for the photocatalytic process. ·OH plays a secondary role while H^+ plays the weakest role. The scavenge experiments were implemented under anaerobic conditions to verify whether the source of $\cdot O_2^-$ is O_2. Results show that the degradation efficiencies of TC for all catalytic materials are only ~6% without any scavenger. Meanwhile the degradation efficiency is hardly changed after masking $\cdot O_2^-$ and ·OH with BQ and IPA (Figure 5C). These results clearly demonstrate that the dissolved oxygen plays an important role in the degradation process of antibiotics. That is to say, $\cdot O_2^-$ comes from the dissolved oxygen. Furthermore, when the h^+ is quenched by TEA, the degradation efficiency is decreased significantly. Thus, even though the degradation efficiency is very low under the anaerobic conditions, h^+ still play an important role in this process.

2.3. Inactivation of *E. coli* HB101 and Damage of ARGs

The accumulation of antibiotics in the water environment may make bacteria resistant to antibiotics, named ARB. The presence of ARB will reduce the effectiveness of therapeutic drugs and pose potential risks to ecosystems and human safety.[62] Thus, the inactivation experiments of *E. coli* HB101 and damage of ARGs were also investigated in detail by employing the prepared photocatalysts. The results of the control experiments without photocatalyst show that the number of *E. coli* HB101 is only decreased by less than one order of magnitude even in the presence of both visible-light and antibiotics (**Figure 6**A-D). It indicates that the *E. coli* HB101 could not be effectively inactivated in the presence of the visible-light or antibiotics. In contrast, the *E. coli* HB101 is completely inactivated from its initial number of 10^8 CFU·mL^{-1} in 10 min under the visible-light *via* the action of as-designed CM/Cu_2O@FeO-nanoarrays (Figure 6E), whilethe other catalysts could completely inactivate *E. coli* HB101 in 50 minutes with their inactivation orders of CM/Cu_2O@Fe_2O_3 > CM/Cu_2O@Fe > CM/Cu_2O. Compared with the reported works for the inactivation efficiency of ARB corresponding to the *E. coli*, the inactivation performance of CM/Cu_2O@FeO-

nanoarrays in this study has greater advantages (Table S4, SI). ARGs not only spread vertically *via* heredity, but also transfer horizontally from one bacterium to another.[63] Thus, the damage of ARGs is of great significance to reduce antibiotic pollution. Under the visible-light irradiation, the damage efficiencies of CM/Cu_2O@FeO-nanoarrays are 3.3 log_{10} for *tetA* (*vs.* TC), 3.4 log_{10} for *aphA* (*vs.* KAN), and 4.4 log_{10} for *tnpA* (*vs.* AMP) with the initial concentrations 2.2 × 10^8, 4.2 × 10^8, and 4.2 × 10^8 copies·mL^{-1} after 180 min, respectively (Figure 6F).

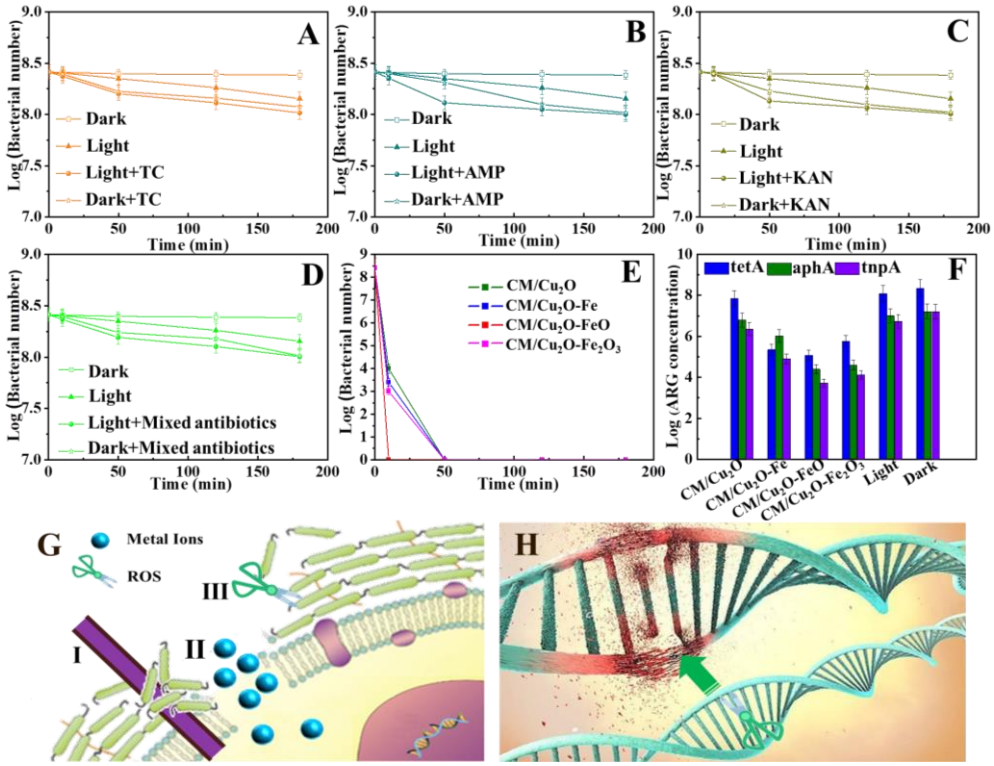

Figure 6. (A) - (D) Inactivation of *E. coli* HB101 without photocatalyst; Inactivation of *E. coli* HB101 (E) and damage of ARGs (F) by photocatalysts under visible-light; The illustrated mechanism of inactivating *E. coli* HB101 (G) and degrading ARGs (H) by CM/Cu_2O@FeO-nanoarrays.

Figure 6G shows the proposed mechanisms of inactivating *E. coli* HB101 and degrading of ARGs. There are three factors which are contributed to excellent inactivation performance of CM/Cu_2O@FeO. (I) is the process of inactivating *E. coli* HB101 by the physical action of 1D nanoarray structure. 1D nanostructured materials have sharp tips. When they come into

contact with bacteria, the cell membrane will be pierced causing the content to flow out and then be killed. This is similar to the nanorod array structure on the surface of cicada wings, which is like neatly arranged steel needles, resulting in mechanical rupture of the cell wall of bacterial.[24] The main component of the cell wall of *E. coli* HB101 is peptidoglycan. Moreover, the thickness of cell wall of *E. coli* HB101 is only about 11 μm which is less than the length of the obtained nanoarrays (25 μm). Because the area of bacteria attached to the surface of nanoarray is much smaller than its suspended part, the cell wall and cell membrane of *E. coli* can be penetrated and destroyed under the combined action of gravity and the nanostructure of nanoarrays.[64] (II) is the metal ions accumulated on the surface, which will destroy the function of cell membrane and enter the cell interior. This will cause the release of some cell contents, which could interfere the cell metabolism process or the function of various enzymes.[65-67] They might ultimately cause the cell death. In the photocatalytic process, the concentration of metal ions dissolved from the as-design materials are listed in Table S5. The results show that the dissolution amount of copper ions is far below the limit of 1.0 $mg \cdot L^{-1}$ in the "Guidelines for drinking-water quality". While there is no iron ion detected, because the cell membrane might have adsorption or wrapping effects on iron ions. (III) is the crucial role of ROS for the inactivation of pathogens. Cho et al.[68] found a linear correlation between hydroxyl radicals and the inactivation of *E. coli*. To date, the most convincing mechanism of ROS inactivation to bacteria shows that lipids are the major attack targets for ROS generated in the extracellular environment.[69,70] Because the phospholipid membranes are predominantly composed of a repeatedly arranged lipids, they may be susceptible to peroxidation. The radical chain reactions initiated by the ROS causes the damages of the cells at sites relatively distant from the initiation source. This occurs because the reaction of an unsaturated fatty acid with a radical in the presence of oxygen leads to the formation of a peroxyl radical which can react with other nearby lipid molecules to generate additional lipid radicals.[71] This process continues as these newly formed lipid radicals react with the other

unsaturated lipids. These chain reactions eventually result in the oxidation of biomolecules at sites considerably far away from where the initial free radical reaction occurred.[72] The damage process of ARGs is illustrated in Figure 6H. The ARGs are particularly susceptible to oxidative stress. The ROS produced by photocatalysts may attack DNA either at the sugar chains or at the bases, which ultimately leads to sugar fragmentation and base loss.[73]

2.4. Synchronization for inactivation of *E. coli* HB101 and damage of ARGs & antibiotics

In the real water environment, antibiotics, ARB, and ARGs are co-existed as a whole.[74] Therefore, it is very important to study the performance of catalyst in the presence of these three pollutants. We have prepared the mixed solution environment containing antibiotics (TC, AMP, and KAN) and *E. coli* HB101 in order to investigate the combined effects of inactivation, degradation and damage. The degradation efficiencies of antibiotics in the presence of *E. coli* HB101 are displayed in **Figures 7**A-C. The CM/Cu_2O@FeO-nanoarrays exhibits the best degradation efficiencies of 92%, 92%, and 93% (corresponding to degradation rate of -0.019, -0.012, and -0.022 min^{-1}, Figure S5 and Table S6, SI) for TC, AMP, and KAN within 180 min, respectively. The detail degradation efficiencies are 87%, 84%, 62% for TC, 85%, 80%, 54% for AMP, and 87%, 84%, 78% for KAN by using CM/Cu_2O@Fe_2O_3, CM/Cu_2O@Fe, and CM/Cu_2O as photocatalysts within 180 min. The degradation of antibiotics is confirmed by a designed experiment, in short, failure analysis test in which TC as a typical example (Figure 7D). The proliferation of *E. coli* ATCC 25922 can be effectively inhibited in 1~4 mg·L^{-1} TC solution.[75,76] The results exhibit that there are few *E. coli* alive in the LB broth with original 50 mg·L^{-1} TC or visible-light irradiated 50 mg·L^{-1} TC solution. Conversely, the number of *E. coli* ATCC 25922 in the LB broth with 50 mg·L^{-1} TC solution which is inactivated by CM/Cu_2O@FeO under visible-light for 3 h, reaches ~2 × 10^4 CFU·mL^{-1} and 3 × 10^7 CFU·mL^{-1} after proliferation in 37 °C for 4 h and 20 h, respectively, which is to those of positive control. The above results suggest that the TC is

degraded at least to < 1 mg/L. Inset of Figure 7D depicts the TC degradation in terms of total organic carbon (TOC) removal for CM/Cu_2O@FeO-nanoarrays over different times. The decomposition efficiency reached about 39.82% within the irradiation time of 25 min. When the irradiation time was lengthened to 120 and 180 min, the TOC removal increased to 72.71% and 78.45%. Hence, CM/Cu_2O@FeO-nanoarrays could effectively mineralize TC into small intermediates or directly CO_2 and H_2O, and it is validated a promising application potential for antibiotics treatment.

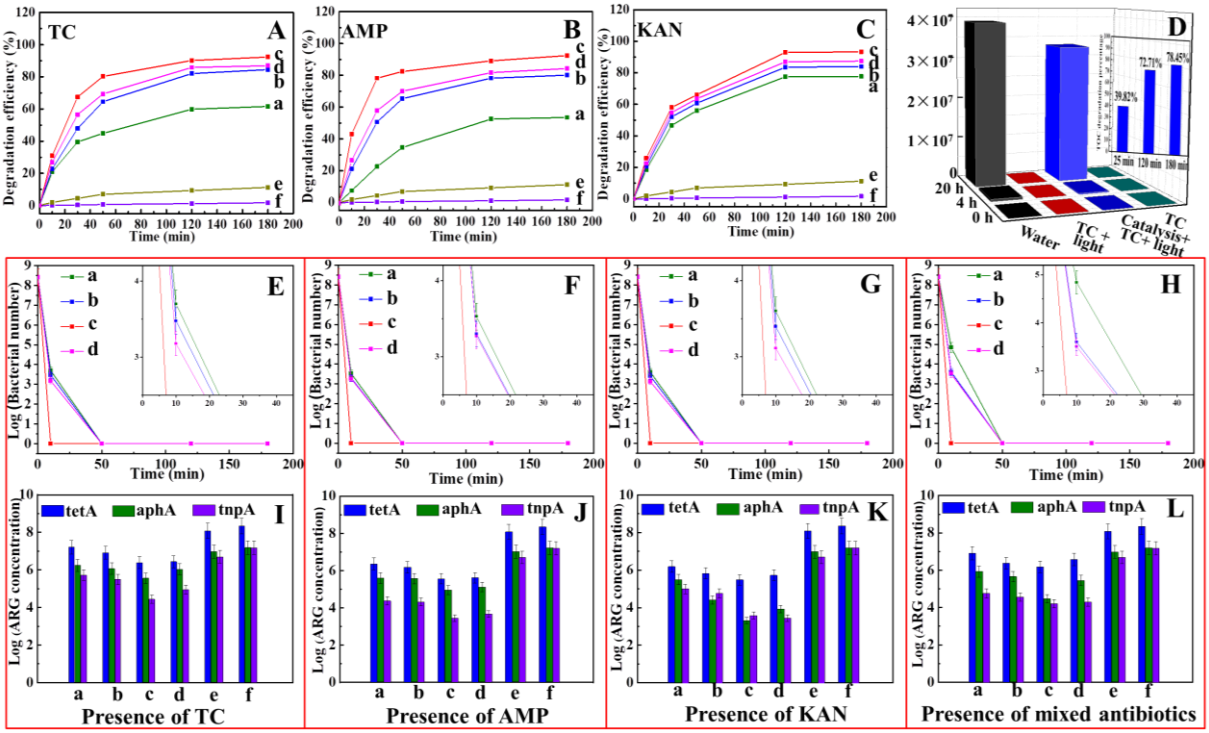

Figure 7. The degradation efficiency of TC (A), AMP (B), and KAN (C); TOC removal efficiencies of TC for CM/Cu_2O@FeO over different times; (E-H) Inactivation of *E. coli* HB101; (I-L) Damage of ARGs for CM/Cu_2O (a), CM/Cu_2O@Fe (b), CM/Cu_2O@FeO (c), CM/Cu_2O@Fe_2O_3 (d), visible-light irradiation without catalysis (e), and dark without catalysis (f).

Figures 7E-H clearly indicate that the CM/Cu_2O@FeO-nanoarrays is the superior antibacterial material for *E. coli* HB101 in 10 min in the presence of antibiotics, compared with those of CM/Cu_2O@Fe_2O_3, CM/Cu_2O@Fe, and CM/Cu_2O with an inactivation time of

50 min. Meanwhile, the overall damage efficiency of ARGs is maintained 3 $\log_{10}$ by CM/Cu_2O@FeO-nanoarrays in the antibiotics solution environment (Figures 7I-L**)**. The changes in the synchronization with inactivation of *E. coli* HB101 and damage of ARGs & antibiotics are similar, which show the following trends: CM/Cu_2O@FeO > CM/Cu_2O@Fe_2O_3 > CM/Cu_2O@Fe > CM/Cu_2O. The above results clearly show that the CM/Cu_2O@FeO-nanoarrays has excellent tri-function of degrading antibiotics, damaging ARGs and inactivating ARBs performances under the visible-light.

3. Conclusions

The as-designed trifunctional Cu-Mesh/Cu_2O@FeO-nanoarrays is prepared *via* GPT process, which is considered a promising aspect of inactivating *E. coli* HB101 and degrading ARGs & antibiotics. Results show that the CM/Cu_2O@FeO-nanoarrays exhibits not only the optimal photocatalytic properties for a single antibiotic contaminant, but also high degradation efficiencies up to 90% in 180 min for three antibiotics. More than 3 $\log_{10}$ of ARGs are damaged. The *E. coli* HB101 can be inactivated up to 100% in 10 min in presence of antibiotic environment. Among contrast samples, the superior degradation efficiency of CM/Cu_2O@FeO is due to it has a suitable conduction band position for converting O_2 into $\cdot O_2^-$. Especially, the important role of dissolved oxygen in solution in the generative process of $\cdot O_2^-$ is proved by scavenge experiments under anaerobic conditions. For the inactivation of *E. coli* HB101, the CM/Cu_2O@FeO-nanoarrays could largely enhance the antimicrobial activity with tip effect of 1D nanostructure and its ROS generation. This study provides a green methodology to solve the issue of antibiotics pollution, which is induced by antibiotics, ARB, and ARGs.

4. Experimental section

All the reagents and characterization methods used in the work are listed in Text S4 in the supporting information.

Synthesis methods of trifunctional CM/Cu_2O@FeO-nanoarrays: 2 g NaOH and 0.540 g $(NH_4)_2S_2O_8$ were dissolved in 20 mL distilled water and ultrasonically treated for 20 min. Then a piece of CM with a dimension of 1 cm × 1 cm (which has been ultrasonically cleaned in 1 mol·L^{-1} HCl) was added in the above solution. A few minutes later, faint blue color appeared on the CM surface and the solution gradually became blue. In 40 min, the deep blue film covered the CM surface, and then the CM was taken out to rinse with distilled water and ethanol. The product is CM/$Cu(OH)_2$. Subsequently, the CM/$Cu(OH)_2$ was added in 10 mL $Fe(NO_3)_3$•$9H_2O$ solution (1 mM). The CM/$Cu(OH)_2$ was taken out when the color was changed from blue to green to yellow, which indicates the formation of CM/$Cu(OH)_2$@$Fe(OH)_3$. It was then heated at 450 ℃ for 5 h under a high-purity H_2 gas flow. After cooled down to room temperature, the CM/Cu_2O@FeO-nanoarrys was obtained. CM/Cu_2O, CM/Cu_2O@Fe and CM/Cu_2O@Fe_2O_3 were also prepared as the control group samples and the synthetic methods are given in Text S5, S6 and S7 in the supporting information.

Characterization: The morphologies of materials were observed using a scanning electron microscope (SEM, HITACHIS-4800, Japan). A high resolution transmission electron microscope (HR-TEM, JEM-2100, Japan, with an accelerating voltage of 200 kV) was used to characterize the crystal lattice spacing. Energy-dispersive X-ray spectroscopy (EDS) was employed to obtain the elemental information at 20 keV. X-ray diffractometer (XRD, D/max-RB, Germany) with a Cu Kα radiation source (γ = 0.154056 nm) was applied to obtain diffraction patterns at 2θ=10-80° with the scanning rate of 0.05°·s^{-1}. X-ray photoelectron spectroscopy (XPS, PHI-5000C ESCA, America) with Al Kα radiation (*hv* = 1486.6 eV) was used to characterize the valence information. Raman spectra were obtained using an inVia Raman spectroscopy (Renishaw, U.K.) with He-Ne laser at λ = 514 nm and power = 10~20 mW. The band gaps of the samples were detected using a UV-vis diffuse reflectance (Cary

5000 UV-Vis-NIR, America) with a Pb smart detector at the measurement range of 350~750 nm.

Photocatalytic tests of antibiotics: Photocatalytic tests of TC, AMP, and KAN were carried out on the equipment (Figure S6, SI) with recirculating cooling system, visible-light irradiation system (150 W Xenon lamp, $\lambda > 400$ nm), sample placement system and light filter system. The CM/Cu_2O@FeO-nanoarrays and the control group samples were loaded into a quartz test tube with a antibiotic solution (10 $mg \cdot L^{-1}$). The dosage of photocatalyst was determined by the optimization results which are shown in Figure S7. When the number of CM/Cu_2O@FeO-nanoarrays is more than 4 pieces, the time for it to reach the maximum degradation efficiency does not change. Therefore, the dosage of photocatalyst is 4 pieces in the work. Before the irradiation experiments under the visible-light, the antibiotic solutions were magnetically stirred for 30 min in the dark environment. The concentrations of antibiotics during the degradation processes were determined by simple spectrophotometric methods, which are summarized in the S8. In order to determine the contribution of ROS, radical trapping experiments were conducted by adding diverse scavengers into a mixed solution of antibiotics and *E. coli* HB101, including triethanolamine (TEA, 1mM), benzoquinone (BQ, 0.01 mM) or isopropanol (IPA, 1 mM). And then, the same operation as described in S8 was performed.

Antibacterial assay: By far the most studied bacteria in the literature is *E. coli*, which is an indicator micro-organism in the drinking water. The stock bacteria solution was prepared as follows. The strains were cultured in a Luria-Bertani broth (10 $g \cdot L^{-1}$ peptone, 5 $g \cdot L^{-1}$ yeast extract, 5 $g \cdot L^{-1}$ NaCl, pH = 7.3±0.2) with 500 $mg \cdot L^{-1}$ tetracycline hydrochloride, 600 $mg \cdot L^{-1}$ ampicillin trihydrate and 800 $mg \cdot L^{-1}$ kanamycin sulfate in an incubator for overnight at 37±1°C. Then 30 mL as-prepared bacteria were centrifuged and washed by 0.9% NaCl for three times. Afterwards, they were diluted to 30 mL by 0.9% NaCl. Then the number of the cultivable bacteria was measured using a plate method. The plate was prepared by LB Agar

(10 g·L^{-1} peptone, 15 g·L^{-1} agar, 10.5 g·L^{-1} NaCl, 5 g·L^{-1} yeast extract, pH = 7.23±0.20) with 500 mg·L^{-1} tetracycline hydrochloride, 600 mg·L^{-1} ampicillin trihydrate and 800 mg·L^{-1} kanamycin sulfate. After the bacterial number determined, the same method for culture and washing was used to prepare 30 mL stock bacteria solution. The stock bacteria solution should be used in less than 3 hours, and its number should be also measured as the initial bacteria number. Traditional surface plating method was used to determine the viable cell number. Four pieces of CM/Cu_2O@FeO-nanoarrays were added into ~10^8 CFU·mL^{-1} *E. coli* HB101 0.9% NaCl solution for visible-light irradiation with slight magnetic stirring, then the number of bacterial at 0, 10, 50, 120, 180 min were examined by ten-fold volume dilution. The antibacterial activity of the CM/Cu_2O@FeO-nanoarrays was evaluated and compared with the other control groups including CM/Cu_2O, CM/Cu_2O@Fe and CM/Cu_2O@Fe_2O_3 toward the inactivation efficiency on *E. coli* HB101. All the experiments were conducted in triplicate and the average values were used.

ARGs extraction and real-time quantitative polymerase chain reaction (qPCR): After 180 min reaction, 10 mL of final solution was collected for ARGs detection. Firstly, 10 mL of the final solution was centrifuged at 12000 rpm for 1 min, then the supernatant was discarded. After this process, the genes of *E. coli* HB101 from the precipitation were extracted following the instructions of TIANprep Mini Plasmid Kit. The final plasmid was stored at -20 ℃ for one week before analysis. Before the ARGs analysis, 10 μL TB Green premix Ex Taq (Tli RNaseH Plus) (2X), 0.4 μL of 10 μM PCR Forward Primer, 0.4 μL of 10 μM PCR Reverse Primer, 0.4 μL ROX Reference Dye II (50X), 6.8 μL sterile water and 2.0 μL sample DNA were mixed for qPCR. The reaction sequence is as follows: initial denaturation at 94 ℃, 1 min at 60 ℃ and the 15 s at 75 ℃; and a final amplification for 15 s at 72 ℃ and 1 min at 60 ℃. The sterile water was used for blank control in each qPCR run. The standard curves were also obtained using the same method with different ARGs concentrations. The standard sequence of *tetA*, *aphA* and *tnpA* were extracted and cloned after checking by Sangon Biotech.

And the sequences of primers for *tetA, aphA* and *tnpA* were listed in Table S7. Because the gene damaged by free radicals cannot be detected, the amount of gene damage can be obtained through the predetermined standard curves of concentration and CT value. And the standard curves of *tetA, aphA* and *tnpA* are shown in Figure S8.

Supporting Information

Supporting Information is available from the Wiley Online Library or from the author.

Acknowledgement

This work was financially supported by the National Natural Science Foundation of China (NSFC Nos: 22171212, 21771140, 51771138, 51979194), International Corporation Project of Shanghai Committee of Science and Technology by China (No. 21160710300), International Exchange Grant (IEC/NSFC/201078) through Royal Society UK and NSFC. We also thank the research on water quality stability characteristics and countermeasures of the Fuzhou Water Supply System (Project No. 20203000) from Fuzhou Water Group Co. Ltd. Author 1 (Long Zhao) and Author 2 (Wei Zhou) contributed equally to this work.

Conflicts of interest

The authors declare no conflict of interest.

Received: (will be filled in by the editorial staff)

Revised: (will be filled in by the editorial staff)

Published online: (will be filled in by the editorial staff)

References

[1] H. Chen, L. Jing, Y. Teng, J. Wang, *Sci. Total Environ.* **2018**, *618*, 409.

[2] Y. C. Deng, J. Liu, Y. B. Huang, M. M. Ma, K. Liu, X. M. Dou, Z. J. Wang, S. C. Qu, Z. G. Wang, *Adv. Funct. Mater.* **2020**, *30*, 2002353

[3] M. Kumar, B. Ram, H. Sewwandi, S. Sulfikar, C. G. G. Tushara, *Environ. Res.* **2020**, *183*, 109179.

[4] F. Triggiano, C. Calia, G. Diella, M. T. Montagna, G. Caggiano, *Microorganisms* **2020**, *8*, 1567.

[5] H. Kim, S. Lee, H. W. Seo, B. Kang, J. Moon, K. G. Lee, D. Yong, H. Kang, J. Jung, E. K. Lim, J. Jeong, H. G. Park, C. M. Ryu, T. Kang, *ACS Nano* **2020**, *14*, 17241.

[6] E. W. Rice, P. Wang, A. L. Smith, L.B. Stadler, *Environ. Sci. Technol. Lett.* **2020**, *7*, 282.

[7] Y. Hu, Y. L. Li, J. Y. He, K. S. Zhang, T. Liu, X. J. Huang, L. T. Kong, J. H. Liu, *J. Environ. Manage.* **2019**, *245*, 291.

[8] B. B. Shao, Z. F. Liu, G. M. Zeng, Z. B. Wu, Y. Liu, M. Cheng, M. Chen, Y. J. Liu, W. Zhang, H. P. Feng, *ACS Sustainable Chem. Eng.* **2018**, *6*, 16424.

[9] S. F. An, G. H. Zhang, T. W. Wang, W. N. Zhang, K. Y. Li, C. S. Song, J. T. Miller, S. Miao, J. H. Wang, X. W. Guo, *ACS Nano* **2018**, *12*, 9441-9450.

[10] Y. Chen, G. Zhang, H. Liu, J. Qu, *Angew. Chem. Int. Ed.* **2019**, *58*, 8134.

[11] M. Shi, H. S. Kwon, Z. M. Peng, A. Elder, H. Yang, *ACS Nano* **2012**, *6*, 2157.

[12] Y. Lin, C. P. Yang, S. H. Wu, X. Li, Y. J. Chen, W. L. Yang, *Adv. Funct. Mater.* **2020**, *30*, 2002918.

[13] H. X. Dai, W. S. Choe, C. K. Thai, M. Sarikaya, B. A. Traxler, *J. Am. Chem. Soc.* **2005**, *127*, 15637.

[14] C. H. Kuo, C. H. Chen, M. H. Huang, *Adv. Funct. Mater*. **2007**, *17*, 3773.

[15] K. Giannousi, G. Sarafidis, S. Mourdikoudis, A. Pantazaki, C. Dendrinou-Samara, *Inorg. Chem.* **2014**, *53*, 9657.

[16] A. Nath, A. Das, L. Rangan, A. Khare, *Sci. Adv. Mater.* **2012**, *4*, 106.

[17] C. Y. Wu, S. G. Wang, J. L. Zhao, Y. Y. Liu, Y. T. Zheng, Y. Luo, C. Q. Ye, M. X. Huang, H. R. Chen, *Adv. Funct. Mater*. **2019**, *29*, 1901722.

[18] C. Y. Toe, J. Scott, R. Amal, Y. H. Ng, *J. Photoch. Photobio. C* **2019**, *40*, 191.

[19] W. W. Xia, J. W. Sun, X. H. Zeng, P. D. Wang, M. Luo, J. Dong, H. G. Yu, *ACS Omega* **2020**, *5*, 2205.

[20] T. K. Townsend, E. M. Sabio, N. D. Browning, F. E. Osterloh, *Energy Environ. Sci.* **2011**, *4*, 4270.

[21] J. A. Niu, J. Albero, P. Atienzar, H. García, *Adv. Funct. Mater*. **2020**, *30*, 1908984.

[22] J. L. Xie, C. X. Guo, C. M. Li, *Energy Environ. Sci.* **2014**, *7*, 2559.

[23] J. Y. Tang, Z. Y. Huo, S. Brittman, H. W. Gao, P. D. Yang, *Nat. Nanotechnol.* **2011**, *6*, 568.

[24] F. D. Xue, J. J. Liu, L. F. Guo, L. R. Zhang, Q. Z. Li, *J. Theor. Biol.* **2015**, *385*, 1.

[25] N. Zhao, Z. Wang, C. Cai, H. Shen, F. Y. Liang, D. Wang, C. Y. Wang , T. Zhu, J. Guo, Y. X. Wang, X. F. Liu, C. T. Duan, H. Wang, Y. Z. Mao, X. Jia, H. X. Dong, X. L. Zhang, J. Xu, *Adv. Mater.* **2014**, *26*, 6994.

[26] Y. K. Tian, A. J. Huang, Z. G. Wang, M. K. Wang, Q. S. Wu, Y. Shen, Q. J. Zhu, Y. Q. Fu, M. Wen, Chem. Eng. J. **2021**, *426*, 131827.

[27] H. Fang, J. H. Yang, M. Wen, Q. S. Wu, *Adv. Mater.* **2018**, *30*, 1705698.

[28] C. W. Cheng, H. J. Fan, *Nano Today* **2012**, *7*, 327.

[29] G. T. Zan, T. Wu, F. Zhu, P. F. He, Y. P. Cheng, S. S. Chai, Y. Wang, X. F. Huang, W. X. Zhang, Y. Wan, X. J. Peng, Q. S. Wu. *Matter,* **2021**, DOI:10.1016/j.matt.2021.07.021.

[30] G. T. Zan, Q. S. Wu. *Adv. Mater.* **2016**, *28*, 2099.

[31] Z. Fang, Y. F. Liu, Y. T. Fan, Y. H. Ni, X. W. Wei, K. B. Tang, J. M. Shen, Y. Chen, *J. Phys. Chem. C* **2011**, *115*, 13968.

[32] C. C. Hou, W. F. Fu, Y. Chen, *ChemSusChem* **2016**, *9*, 2069.

[33] O. Lupan, L. Chow, G. Chai, H. Heinrich, *Chem. Phys. Lett.* **2008**, *465*, 249.

[34] N. He, X. F. Yang, L. X. Shi, X. C. Yang, Y. Lu, G. X. Tong, W. H. Wu, *Carbon* **2020,** *166*, 205.

[35] A. D. Sekar, T. Jayabalan, H. Muthukumar, N. I. Chandrasekaran, S. N. Mohamed, M. Matheswaran, *Energy* **2019**, *172*, 173.

[36] J. C. Wang, L. Zhang, W. X. Fang, J. Ren, Y. Y. Li, H. C. Yao, J. S. Wang, Z. J. Li, *ACS Appl. Mater. Interfaces* **2015**, *7*, 8631.

[37] S. Munir, A. R. Varzeghaniab, S. Kaya, *Sustain. Energy Fuel.* **2018**, *2*, 2532.

[38] Y. Su, H. F. Li, H. B. Ma, H. Wang, A. Nathan, *ACS Omega* **2018**, *3*, 1939.

[39] Y. Mendili, J. F. Bardeau, N. Randrianantoandro, F. Grasset, J. M. Greneche, *J. Phys. Chem. C* **2012**, *116*, 23785.

[40] W. Yang, Y. Wang, *Appl. Catal. B* **2021**, *282*, 119574.

[41] Y. K. Zheng, L. Zhang, J. Guan, S. Y. Qian, Z. X. Zhang, C. K. Ngaw, S. L Wan, S. Wang, J. D. Lin, Y. Wang, *ACS Sustainable Chem. Eng.* **2021**, *9*, 1754.

[42] Y. X. Zhao, L. L. Fan, Y. Zhang, H. Zhao, X. J. Li, Y. P. Li, L. Wen, Z. F. Yan, Z. Y. Huo, *ACS Appl. Mater. Interfaces* **2015**, *7*, 16802.

[43] Z. Wang, M. Chen, J. Shu, Y. Li, *J. Alloys Compd.* **2016**, *682*, 432.

[44] J. Pal, A. K. Sasmal, M. Ganguly, T. Pal, *J. Phys. Chem. C* **2015**, *119*, 3780.

[45] Z. Li, J. Liu, D. Wang, Y. Gao, J. Shen, *Int. J. Hydrogen Energy* **2012**, *37*, 6431.

[46] L. Liu, N. He, T. Wu, P. B. Hu, G. X. Tong, *Chem. Eng. J.* **2019**, *335*, 103.

[47] L. Liu, Z. D. He, Y. T. Zhao, J. C. Sun, G. X. Tong, *J. Alloys Compd.* **2018**, *765*, 1218.

[48] Y. Liu, Y. Fu, L. Liu, W. Li, J. G. Guan, G. X. Tong, *ACS Appl. Mater. Interfaces* **2019**, *10*, 16511.

[49] T. Guo, X. B. Tian, *J. Hazard. Mater*. **2019**, *380*, 120877.

[50] F. Su, P. Li, J. Huang, M. Gu, Z. Liu, Y. Xu, *Sci. Rep.* **2021**, *11*, 1.

[51] F. Chen, Q. Yang, J. Sun, F. B. Yao, S. N. Wang, Y. L. Wang, X. L. Wang, X. M. Li, C. G. Niu, D. B. Wang, G. M. Zeng, *ACS Appl. Mater. Interfaces*. **2016**, *8*, 32887.

[52] S. Q. Wu, Y. Lin, Y. H. Hu, *J. Mater. Chem. A* **2021**, *9*, 2592.

[53] G. H. Wang, J. Xiang, J. Y. Lin, L.. Xiang, S. Chen, B. Yan, H. J. Fan, S. J. Zhang, X. W. Shi, *ACS Appl. Mater. Interfaces* **2020**, *12*, 51952.

[54] X. Zhang, X. Wang, J. Chai, S. Xue, R. Wang, L. Jiang, J. Wang, Z. Zhang, D. D. Dionysiou, *Appl. Catal. B* **2020**, *272*, 119017.

[55] N. Shao, Z. A. Hou, H. X. Zhu, J. N. Wang, C. P. Francois-Xavier, *Appl. Catal. B* **2018**, *232*, 574.

[56] H. Wang, J. Zhang, X. Yuan, L. Jiang, Q. Xia, H. Chen, *Chem. Eng. J.* **2020**, *392*, 123638.

[57] S. R. Pendlebury, X. L. Wang, F. L. Formal, M. Cornuz, A. Kafizas, S. D. Tilley, M. Grätzel, J. R. Durrant, *J. Am. Chem. Soc.* **2014**, *136*, 9854.

[58] Y. C. Fu, L. Peng, Q. R. Zeng, Y. Yang, H. J. Song, J. H. Shao, S. Y. Liu, J. D. Gu, *Chem. Eng. J.* **2015**, *270*, 631.

[59] C. Gu, K. G. Karthikeyan, *Environ. Sci. Technol.* **2005**, *39*, 2660.

[60] M. Sakamoto, K. Inoue, M. Saruyama, K. Kimoto, M. Okano, Y. Kanemitsu, T. Teranishi, *Chem. Sci.* **2014**, *5*, 3831.

[61] S. J. Li, S. Hu, W. Jiang, J. L. Zhang, K. B. Xu, Z. H. Wang, *J. Colloid. Interf. Sci.* **2019**, *556*, 335.

[62] M. Hwangbo, E. C. Claycomb, Y. N. Liu, T. E. G. Alivio, S. Banerjee, K. H. Chu, *Sci. Total. Environ.* **2019**, *649*, 1189.

[63] F. H. Wang, M. Qiao, Z. E. Lv, G. X. Guo, Y. Jia, Y. H. Su, Y. G. Zhu, *Environ. Pollut.* **2014**, *184*, 247.

[64] E. P. Ivanova, J. Hasan, H. K. Webb, V. K. Truong, G. S. Watson, J. A. Watson, V. A. Baulin, S. Pogodin, J. Y. Wang, M. J. Tobin, C. Löbbe, R. J. Crawford, *Small* **2012**, *8*, 2489.

[65] X. J. Guo, X. S. He, C. W. Li, N. X. Li, *J. Hazard. Mater.* **2019**, *365*, 457.

[66] S. Meghana, P. Kabra, S. Chakraborty, N. Padmavathy, *RSC Adv.* **2015**, *5*, 12293.

[67] W. Zhou, L. Fu, L. Zhao, X. J. Xu, W. Y. Li, M. Wen, Q. S. Wu, *ACS Appl. Mater. Interfaces* **2021**, *13*, 10878.

[68] M. Cho, H. Chung, W. Choi, J. Yoon, *Water Res.* **2004**, *38*, 1069.

[69] M. D. Bai, Z. T. Zhang, M. D. Bai, B. Yang, X. Y. Bai, *Plasma Sci. Technol.* **2007**, *9*, 206;

[70] I. Tejero, A. Gonzalez-Lafont, J. M. Lluch, L. A. Eriksson, *J. Phys. Chem. B* **2007**, *111*, 5684.

[71] O. K. Dalrymple, E. Stefanakos, M. A. Trotz, D. Y. Goswami, *Appl. Catal. B* **2010**, *98*, 27.

[72] N. Porter, S. Caldwell, K. Mills, *Lipids* **1995**, *30*, 277.

[73] H. Hidaka, S. Horikoshi, N. Serpone, J. Knowland, *J. Photochem. Photobiol. A* **1997**, *111*, 205.

[74] M. Amarasiri, D. Sano, S. Suzuki, *Crit. Rev. Env. Sci. Tec.* **2020**, *50*, 2016.

[75] L. Migliore, A. Rotini, M. C. Thaller, *Dose-Response* **2013**, *11*, 550.

[76] S.M. Heman-Ackah, *Antimicrob. Agents Ch.* **1976**, *10*, 223.